Pharmacokinetic Analysis of Dynamic ^{18}F-Fluoromisonidazole PET Data in Non–Small Cell Lung Cancer

Jazmin Schwartz[1], Milan Grkovski[1], Andreas Rimner[2], Heiko Schöder[3], Pat B. Zanzonico[1], Sean D. Carlin[3], Kevin D. Staton[3], John L. Humm[1], and Sadek A. Nehmeh[4]

[1]Department of Medical Physics, Memorial Sloan Kettering Cancer Center, New York, New York; [2]Department of Radiation Oncology, Memorial Sloan Kettering Cancer Center, New York, New York; [3]Department of Radiology, Memorial Sloan Kettering Cancer Center, New York, New York; and [4]National Center for Cancer Care and Research, Doha, Qatar

Hypoxic tumors exhibit increased resistance to radiation, chemical, and immune therapies. ^{18}F-fluoromisonidazole (^{18}F-FMISO) PET is a noninvasive, quantitative imaging technique used to evaluate the magnitude and spatial distribution of tumor hypoxia. In this study, pharmacokinetic analysis (PKA) of ^{18}F-FMISO dynamic PET extended to 3 h after injection is reported for the first time, to our knowledge, in stage III–IV non–small cell lung cancer (NSCLC) patients. **Methods:** Sixteen patients diagnosed with NSCLC underwent 2 PET/CT scans (1–3 d apart) before radiation therapy: a 3-min static ^{18}F-FDG and a dynamic ^{18}F-FMISO scan lasting 168 ± 15 min. The latter data were acquired in 3 serial PET/CT dynamic imaging sessions, registered with each other and analyzed using pharmacokinetic modeling software. PKA was performed using a 2-tissue, 3-compartment irreversible model, and kinetic parameters were estimated for the volumes of interest determined using coregistered ^{18}F-FDG images for both the volume of interest–averaged and the voxelwise time–activity curves for each patient's lesions, normal lung, and muscle. **Results:** We derived average values of ^{18}F-FMISO kinetic parameters for NSCLC lesions as well as for normal lung and muscle. We also investigated the correlation between the trapping rate (k_3) and delivery rate (K_1), influx rate (K_i) constants, and tissue-to-blood activity concentration ratios (TBRs) for all tissues. Lesions had trapping rates 1.6 times larger, on average, than those of normal lung and 4.4 times larger than those in muscle. Additionally, for almost all cases, k_3 and K_i had a significant strong correlation for all tissue types. The TBR–k_3 correlation was less straightforward, showing a moderate to strong correlation for only 41% of lesions. Finally, K_1–k_3 voxelwise correlations for tumors were varied, but negative for 76% of lesions, globally exhibiting a weak inverse relationship (average $R = -0.23 \pm 0.39$). However, both normal tissue types exhibited significant positive correlations for more than 60% of patients, with 41% having moderate to strong correlations ($R > 0.5$). **Conclusion:** All lesions showed distinct ^{18}F-FMISO uptake. Variable ^{18}F-FMISO delivery was observed across lesions, as indicated by the variable values of the kinetic rate constant K_1. Except for 3 cases, some degree of hypoxia was apparent in all lesions based on their nonzero k_3 values.

Key Words: non-small cell lung cancer; hypoxia; ^{18}F-fluoromisonidazole; compartmental analysis; pharmacokinetic analysis

J Nucl Med 2017; 58:911–919
DOI: 10.2967/jnumed.116.180422

Lung cancer is the malignancy with the highest mortality for both men and women. Approximately 70% of these patients are diagnosed with nonsquamous non–small cell lung cancer (NSCLC). The 5-y survival of patients treated with surgery alone is 73%, 58%, and 13% for stages IA, IB, and IIIA NSCLC, respectively. Treatment failures are usually associated with distant metastatic recurrences. Even with multimodality treatment (including surgery, chemotherapy, and radiotherapy) in nonresponders to neoadjuvant chemotherapy, the 2-y local control and survival rates are less than 60% (*1*). Tumor hypoxia has been shown to be an independent prognostic marker in several malignancies, including NSCLC (*2*). Hypoxic tumors generally express a more aggressive phenotype and are radioresistant and thus have an increased likelihood of locoregional recurrence, distant metastasis, and poor overall outcome (*3,4*). Nordsmark et al. showed, in fact, that the most predictive factor of survival in head and neck cancer was the proportion of the measurements in each lesion with a $pO_2 < 2.5$ mm Hg; a steep decline in survival was observed when more than 20% of a lesion's measurements had a $pO_2 < 2.5$ mm Hg (*5*). In NSCLC, 38% of patients had lesions, with >20% of the measurements having a $pO_2 < 2.5$ mm Hg (*6*). Potential treatment strategies for overcoming tumor hypoxia and improving local control rates include the use of radiosensitizing drugs and biologic image-guided dose escalation to hypoxic tumor subregions (*7–11*). ^{18}F-fluoromisonidazole (^{18}F-FMISO) PET has been widely investigated as a noninvasive method for detecting tumor hypoxia in several solid tumors, including NSCLC (*2,3*). Rajendran et al., building on previous work in animals by Koh et al., used ^{18}F-FMISO uptake at 120 min after injection to quantify tissue hypoxia; they defined a tumor fractional hypoxic volume (FHV) by including voxels in the tumor image with tissue-to-blood activity concentration ratios (TBRs) > 1.4 (*12,13*). However, the application of ^{18}F-FMISO to assess the FHV in NSCLC has yet to be investigated. Different TBRs and tumor-to-muscle and tumor-to-mediastinum activity concentration ratios (TMRs and TMeRs, respectively) have been proposed as semiquantitative criteria for delineating hypoxic tumor volumes (*3,12–14*); for example,

Received Jul. 7, 2016; revision accepted Oct. 19, 2016.
For correspondence or reprints contact: Jazmin Schwartz, Department of Medical Physics, Memorial Sloan Kettering Cancer Center, 1275 York Ave., New York, NY 10065.
E-mail: schwarj1@mkscc.org
Published online Feb. 23, 2017.

Eschmann et al. showed that a TMeR > 2 was a predictive factor for local recurrence in lung cancer. However, Thorwarth et al. demonstrated that no single ratio threshold in the late ^{18}F-FMISO images may be sufficient to accurately define the spatial distribution of tumor hypoxia (*3,15*). Instead, they suggested that pharmacokinetic analysis (PKA) of dynamic ^{18}F-FMISO PET images should be used to extract local hypoxia and perfusion characteristics of tumor tissue (*15*). In a separate study, Wang et al. argued that the physiologic clearance of ^{18}F-FMISO from highly perfused normal tissue may result in TBRs comparable to those in a tumor at the time of patient imaging (*16*). Eschmann identified 3 types of time–activity curves, representing rapid washout, intermediate or delayed washout, or continuing accumulation, respectively, which correlated with treatment outcome after radiotherapy (*3*). In particular, an accumulation-type curve, a high ^{18}FMISO SUV, and a high TMeR at 4 h after injection were highly suggestive of incomplete response to treatment (*3*).

In this study, we used compartmental modeling to investigate the presence and extent of tumor hypoxia, as measured by ^{18}F-FMISO PET, in a cohort of NSCLC patients, before treatment. In addition, tumor parametric maps of hypoxia surrogate (k_3, K_i, and TBR) and delivery (K_1) metrics were derived and correlations among these parameters evaluated.

MATERIALS AND METHODS

Patients Cohort

Sixteen NSCLC (10 men and 6 women; mean age ± SD, 66 ± 12 y) scheduled for definitive radiation therapy (RT) were included in this study. The institutional review board approved this study, and all subjects signed a written informed consent form. Patient characteristics are summarized in Table 1. The mean tumor volume of the 16 patients included in this study was approximately 18.8 cm^3 (range, 1.7–147.0 cm^3). All patients underwent a pretherapy ^{18}F-FDG PET/CT scan for RT planning. A baseline ^{18}F-FMISO PET/CT scan was then obtained up to 3 d after the ^{18}F-FDG study.

^{18}F-FDG PET/CT

Patients were required to fast for at least 6 h before intravenous injection with 429 ± 16 MBq of ^{18}F-FDG. Patients underwent ^{18}F-FDG PET/CT at 60 ± 10 min after injection while immobilized in an RT simulation cradle. An additional 3-min free-breathing ^{18}F-FDG scan was acquired over 1 PET field of view centered over the primary lesion, followed by a low-dose 4-dimensional CT (120 kVp; 10 mA; tube rotation, 0.5 s). A time-averaged CT (CT_{avg}) was generated retrospectively and used for attenuation correction of free-breathing PET images. PET/CT images were acquired on a Discovery ST PET/CT scanner in 3-dimensional mode (GE Healthcare). PET emission data were corrected for attenuation, scatter, and randoms and iteratively reconstructed using standard clinical parameters (16 subsets, 2 iterations, transaxial postprocessing filter gaussian filter 6.0 mm in full width at half maximum, Heavy 3-point smoothing axially).

^{18}F-FMISO PET/CT

Patients were injected intravenously with an average of 346 ± 33 MBq (range, 242–382 MBq) of ^{18}F-FMISO simultaneously with the start of data acquisition (bolus duration, ~5 s). No fasting was required before the ^{18}F-FMISO injection. The ^{18}F-FMISO was synthesized in our facility using a commercially available cassette (GE Healthcare), with radiochemical purity of at least 95% by high-performance liquid chromatography. The patients were scanned while supine on a flat-top couch insert on a Discovery 690 PET/CT scanner with time of flight (GE Healthcare) and immobilized in the RT simulation cradle. Dynamic ^{18}F-FMISO PET (FMISO-1) acquisition over 1 bed position (centered over the primary lesion) was performed and consisted of 12 × 10, 8 × 60, and 7 × 300 s frames (total duration, 45 min). This was followed by 2 additional 10-min static image acquisitions: FMISO-2 at 95 ± 12 min (range, 79–98 min) and FMISO-3 at 168 ± 15 (range, 146–181 min) after injection. A low-dose 4-dimensional CT (same acquisition parameters as for the ^{18}F-FDG PET/CT study) scan preceded each of the 3 ^{18}FMISO PET sessions; the corresponding CT_{avg} was used for attenuation correction and image registration purposes. All ^{18}F-FMISO PET images were reconstructed using 20 subsets, 2 iterations, transaxial gaussian postprocessing filter 6.4 mm in full width at half maximum, and Heavy 3-point smoothing axially.

TABLE 1
Patient Characteristics

Patient no.	Injected dose (MBq) ^{18}F-FMISO	Injected dose (MBq) ^{18}F-FDG	Sex	Age (y)
1	358	435	F	79
2	336	419	F	75
3	338	411	F	66
4	323	426	F	66
5	367	395	M	33
6	361	419	M	65
7	371	429	M	59
8	336	462	F	65
9	365	441	M	78
10	242	441	M	66
11	349	430	M	71
12	376	429	M	64
13	359	437	F	57
14	382	415	M	60
15	326	450	F	82
16	352	432	M	73
μ ± σ	346 ± 33	429 ± 16		66 ± 11

Image Postprocessing and Preliminary Measurements

The PET tumor volumes from ^{18}F-FDG, FMISO-2, and FMISO-3 were coregistered to that of FMISO-1 by means of their corresponding CT_{avg} images, using the Advantage Workstation rigid registration software tool (version 4.7; GE Healthcare). For patients exhibiting multiple lesions, the registration process and the following processing were performed separately for each lesion. The FMISO-2 and FMISO-3 image sets were decay corrected to the start time of the FMISO-1 acquisition, and then these 3 datasets were merged using PMOD (version 3.609; PMOD Technologies, Inc.) into 1 dynamic image set (^{18}F-FMISO dynamic PET).

Because the heart was within the imaged field of view, image-derived input functions (IFs) were used for this study. Recent work by Nguyen-Kim has shown that, in NSCLC, the bronchial contribution to pulmonary circulation is higher than the pulmonary (*17*). Thus, a volume of interest (VOI) was drawn over the aortic arch on the CT_{avg} image, well within the edges of the structure to avoid spillover effects (Fig. 1A, left), then superimposed on the frames of the ^{18}F-FMISO dynamic PET image set (Fig. 1A, right). The time–activity curves of the 25 VOI voxels with highest activity concentration during the second frame were averaged to obtain the IF (Fig. 1C, green).

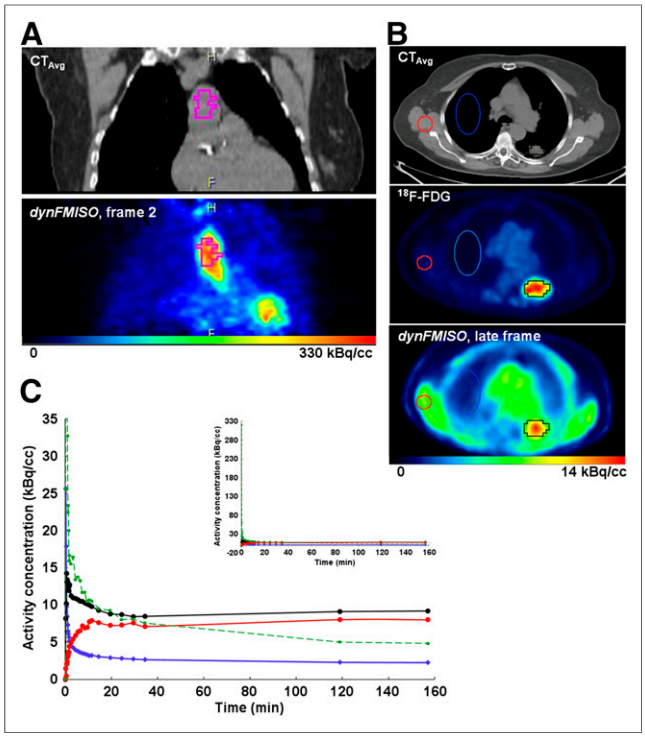

FIGURE 1. Examples of aortic arch VOI (A) and VOI_{Tumor} (black), VOI_{Normal} (blue), and VOI_{Muscle} (red) (B) time–activity curves (C) corresponding to IF (green), *time–activity curve*$_{Avg}$ (black), *time–activity curve*$_{Normal}$ (blue), and *time–activity curve*$_{Muscle}$ (red).

Tumor volumes were delineated on the registered ^{18}F-FDG (Fig. 1B, middle) image and then segmented using a 50%-of-maximum threshold. The background in the ^{18}F-FDG images was at least 10 times smaller than the uptake in the lesions. Thus, it was not necessary to account for it as a caveat for adjusting the threshold. A fused PET/CT image was used to ascertain that the VOI was within the tumor on CT_{avg}. The VOI thus derived, VOI_{Tumor}, was then superimposed on the frames of the ^{18}F-FMISO dynamic PET image set (Fig. 1B, right). Voxelwise time–activity curves were obtained for all voxels within the VOI_{Tumor} and then averaged to provide a mean VOI_{Tumor} time–activity curve (*time–activity curve*$_{Avg}$). Finally, 2 additional VOIs were drawn for each patient: VOI_{Normal}, an ellipsoid drawn over the contralateral normal lung, and VOI_{Muscle}, drawn over muscle in the latissimus dorsi region (Fig. 1B, blue/red, respectively). PKA was performed on the mean time–activity curve of each region (*time–activity curve*$_{Normal}$ and *time–activity curve*$_{Muscle}$, Fig. 1C).

Voxelwise TBRs were calculated for the last frame time, t_{Late}, for each VOI:

$$\text{TBR} = \frac{AC_{Late}}{IF_{Late}}, \qquad \text{Eq. 1}$$

where AC_{Late} and IF_{Late} are the last-frame activity concentrations for a given voxel time–activity curve and IF, respectively. The maximum TBR (TBR_{max}) was then determined. On the basis of previous work, the tumor hypoxic volume (HV) was defined as the volume containing voxels with TBRs > 1.2 (*18*). The FHV was calculated as:

$$\text{FHV} = \frac{\text{HV}}{\text{Lesion volume}}. \qquad \text{Eq. 2}$$

In addition, the time–activity curves of all voxels within the HV were averaged to obtain *time–activity curve*$_{FHV}$ for each lesion and PKA performed of each. For each VOI, the last-frame SUV_{bw} was also calculated:

$$SUV_{bw} = \frac{AC_{Late}}{\text{Injected dose}/_{\text{bw}}}, \qquad \text{Eq. 3}$$

where bw is the body weight (kg). Finally, TMR for each lesion is calculated as $\text{TMR} = LesionTBR/_{MuscleTBR}$.

PKA

The time–activity curve from dynamic PET data, $C_{PET}(t)$, represents the averaged activity concentration in a volume (voxel or VOI) at acquisition time t after injection and is modeled by

$$C_{Model}(t) = (1 - vB) \times (C_1(t) + C_2(t)) + vBC_p(t). \qquad \text{Eq. 4}$$

Every volume, whether a voxel or VOI, is heterogeneous, comprising various tissues and vascular components. The fraction of the vascular space in a volume, *vB,* accounts for the activity arising from the blood within the volume and $(1 - vB)$ represents the fraction of activity in tissue, which is extravascular. The contributions to the measured $C_{PET}(t)$ in a given volume are those from tracer, which is circulating within the plasma (p), ($C_p(t)$); extracted from plasma into tissue and remaining unbound/free ($C_1(t)$); and irreversibly bound, ($C_2(t)$) (*19,20*). Bruehlmeier et al. have shown that the percentage of metabolic degradation of ^{18}F-FMISO is negligible, so metabolite correction

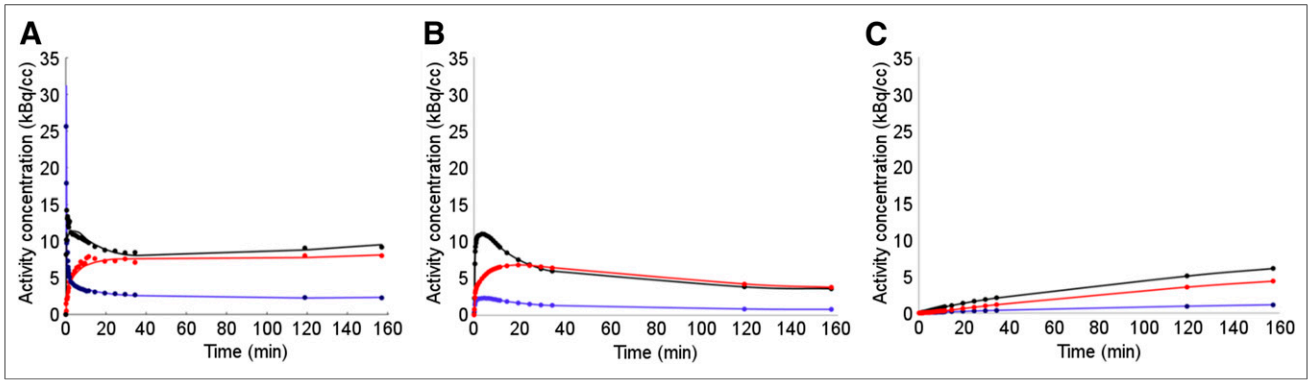

FIGURE 2. Total and compartment time–activity curves for patient 1 VOIs determined by PKA: $C_{model}(t)$ (A), $C_1(t)$ (B), and $C_2(t)$ (C) for *time–activity curve*$_{Avg}$ (black), *time–activity curve*$_{Normal}$ (blue), and *time–activity curve*$_{Muscle}$ (red).

TABLE 2
Statistics of PKA Results for Average Lesion Time–Activity Curves for Each Patient

Data	*vB*	%SE *vB*	K_1 (mL/min/cm^3)	%SE K_1	K_1/k_2	%SE K_1/k_2	k_3 (min^{-1})	%SE k_3	K_i (mL/min/cm^3)	%SE K_i
Average	0.15	20	0.15	11	0.69	3.4	4.1E−03	25	4.1E-03	31
σ	0.10	13	0.06	5.0	0.23	2.1	4.5E−03	27	4.5E-03	26
Minimum	0.01	8.7	0.05	4.2	0.18	1.0	0.0E+00	5.4	0.0E+00	8.3
Maximum	0.45	80	0.25	25	1.10	12	2.1E-02	100	2.1E-02	110

Supplemental Table 1 provides patient/lesionwise results.

is unnecessary. The rate of change of the activity in a given compartment, as a function of time, is a linear combination of the fluxes, scaled by rate constants, into and out of it. This relationship may be described via coupled differential equations:

$$\frac{dC_1(t)}{dt} = k_1 C_p(t) - (k_2 + k_3) C_1(t). \quad \text{Eq. 5}$$

$$\frac{dC_2(t)}{dt} = k_3 C_1(t). \quad \text{Eq. 6}$$

The pharmacokinetic rate constants K_1 and k_2 represent the rate of transport from plasma into and the efflux rate out from the unbound compartment, respectively, whereas k_3 is the rate at which ^{18}F-FMISO is trapped. Therefore, k_3 is often considered a possible surrogate hypoxia metric (*21*).

Modeling was performed using PMOD with a 2-tissue, 3-compartment (plasma, free, bound) model with irreversible binding ($k_4 = 0$). Fitting was performed with Levenberg–Marquardt weighted least-squares optimization to obtain the parameters K_1, k_2, k_3, and *vB* (*22,23*). The weights were obtained by (*16*):

$$w_i = \frac{1}{\sigma_i^2}, \sigma_i = c\sqrt{\left(\frac{C_{PET}(t_i)}{\Delta t_i \times e^{-\lambda t_i}}\right)}, \quad \text{Eq. 7}$$

where c (0.064 as we previously calculated (*24*)) is the scaling factor, Δt_i the frame duration, C_{PET} (t_i) the decay-corrected activity concentration at time t_i, and $\lambda = \ln(2)/T_{1/2}$ the decay constant.

The PKA results were compared for tumor, normal lung, and muscle VOIs voxelwise and averaged over the whole target volume (i.e., *time–activity curve*$_{Avg}$). The influx rate ($K_i = k_1k_3/(k_2 + k_3)$) was also calculated, because it has been suggested as a possible surrogate measure of hypoxia (*16,21,25*).

RESULTS

Figure 2A shows representative model curves, $C_{Model}(t)$, and the corresponding unbound and trapping compartment curves, $C_1(t)$ and $C_2(t)$ (Figs. 2B and 2C, respectively), for VOI_{Tumor} (black), VOI_{Normal} (blue), and VOI_{Muscle} (red) average time–activity curves, respectively.

PKA results for the tumors' *time–activity curve*$_{Avg}$ for the 16 patients (34 lesions) and values of TBR, lesion volume, and maximum SUV_{bw} are tabulated in Tables 2 and 3 and Supplemental Tables 1 and 2 (supplemental materials are available at http://jnm.snmjournals.org). The average values (μ) and corresponding SD and ranges for each parameter were $vB = 0.15 \pm 0.10$ (range, 0.01–0.45); $K_1 = 0.15 \pm 0.06$ (range, 0.05–0.25) mL/min/cm^3; $K_1/k_2 = 0.69 \pm 0.23$ (range, 0.18–1.14); and $k_3 = 0.0041 \pm 0.0045$ (range, 0.00–0.021) min^{-1}. The average TBR across lesions was 1.80 ± 1.45 (range, 0.54–7.97). The results for normal lung and muscle are summarized in Tables 4 and 5 (also Supplemental Tables 3 and 4). Results for all tissues are summarized and compared in Figure 3.

To elucidate the general relationships between k_3 and other parameters across patients, scatterplots were constructed for k_3 of *time–activity curve*$_{Avg}$ (tumor) versus the remaining PKA parameters as well as versus K_i and TBR, for each tissue VOI analyzed (Fig. 4); each data point represents 1 lesion (there is only 1 VOI per patient for normal lung or muscle). The corresponding Pearson correlation coefficients (R) are given in Table 6. A strong correlation was defined as $R > 0.75$, a weak one as $R < 0.5$, and all others as moderate.

For tumors' *time–activity curve*$_{Avg}$, K_1 versus k_3 results show a weak negative correlation ($R = -0.17$), in contrast to what is observed for normal lung ($R = 0.58$) and muscle ($R = 0.28$). Additionally, Table 6 also shows R for k_3 versus K_i and TBR, which are of interest because these parameters have all been proposed as possible hypoxia indices. This is supported by the degree of concordance between these parameters in tumor ($R = 0.84$ for TBR–k_3 and $R = 0.91$ for K_i–k_3); these correlations are highly significant ($P < 0.001$). Interestingly, R is even larger (0.97 and 0.95, $P < 0.001$) in the case of the normal tissues studied.

Table 7 summarizes the results of voxelwise correlations calculated between k_3 and the foregoing parameters for each VOI (also Supplemental Table 5). Variable voxelwise correlations between K_1 and k_3 were observed for lesion VOIs (−0.97–0.72 and $R < 0$ in 24 out 34 lesions, 20 of which were significant, with $P < 0.001$), which averaged across lesions depicts a weak inverse relationship (average $R = -0.23 \pm 0.39$). For both normal tissues, R for K_1–k_3 was positive for 81% of normal lung (75% with $P < 0.05$) and 75% of muscle (50% with $P < 0.05$) patients; 13% (lung) and 44% (muscle) of those exhibited moderate to high correlations ($R > 0.5$).

TABLE 3
Statistics of Quantitative Lesion Parameters for Each Tumor VOI and Patient

Data	SUV_{max}	TBR	Volume (cm^3)	FHV
Average	3.0	1.8	19	39
σ	2.2	1.5	27	43
Minimum	1.1	0.54	1.7	0.0
Maximum	13	8.0	150	100

Supplemental Table 2 provides patient/lesionwise results.

TABLE 4
PKA Results for Average Normal Lung Time–Activity Curves

Data	*vB*	%SE *vB*	K_1 (mL/min/cm^3)	%SE K_1	K_1/k_2	%SE K_1/k_2	k_3 (min^{-1})	%SE k_3	SUV_{max}	TBR
Average	0.16	14	0.029	26	0.17	12	1.8E−03	23	1.1	0.7
σ	0.063	9.7	0.019	14	0.052	6.8	2.4E−03	9.3	0.5	0.2
Minimum	0.064	6.2	0.0061	15	0.079	5.9	0.0E+00	12	0.4	0.3
Maximum	0.27	41	0.068	71	0.25	32	8.2E-03	33	2.2	1.1

Supplemental Table 3 provides patient/lesionwise results.

The influx rate constant, K_i, which has been proposed as a surrogate measure for hypoxia, showed a positive correlation with k_3 in 33 of 34 tumors, 31 of which had an $R > 0.5$ ($P < 0.001$). Likewise, 100% of the patients had a K_i–k_3 $R > 0.5$ for normal lung and muscle. As $k_2 >> k_3$, it is possible to deduce that $K_i \cong K_1 \times k_3/k_2$. The highly positive correlation between K_i and k_3 in all 3 tissue types is therefore as expected. For 71% of lesions, TBR–k_3 had an $R > 0$ and 53% showed moderate to strong correlations ($P < 0.001$), likewise for both normal lung and muscle tissues. Finally, 67% of lesions had nonzero FHVs. Of these, 38% had an FHV > 0.5 (half the tumor volume).

Finally, plotting the K_1–k_3 voxelwise R versus the lesion's respective average k_3 shows that as the lesion becomes less hypoxic (as indicated by k_3), the correlation between delivery and trapping becomes more positive (Fig. 5).

To increase the statistical power of the correlations, a similar analysis was carried by first grouping voxels into k_3-deciles using the voxelwise parametric maps. Supplemental Figures 1A and 1B show bar graphs of R for K_1–k_3 for the respective results from normal lung and muscle; each bar corresponds to 1 patient (as does the color for comparison to tumor results because several patients had multiple lesions). Supplemental Figure 1D shows a similar plot for the decilewise analysis; in this case, each bar represents a lesion (each color a patient as in A and B). Eighty-eight percent of the lesions had an $R < 0$ for K_1–k_3, 59% of which had moderate to strong anticorrelations. Supplemental Figure 1C shows the same figure for the voxelwise results discussed in the previous section, for comparison. Figure 6 shows that as the TBR decreases, the R for K_1–k_3 changes from $R < 0$ to $R > 0$. Similar results were found for TMR (Supplemental Fig. 2).

Finally, PKA of the *time–activity curve*$_{FHV}$ showed that for only 8 of 23 lesions k_3 was significantly different ($P < 0.05$) from that of *time–activity curve*$_{Avg}$. Of those 8, only 5 had a k_3 higher than that of *time–activity curve*$_{Avg}$. Additionally, in every case, the maximum TBR in HV was larger than the TBR for the voxel with the maximum k_3. Moreover, the maximum k_3 voxel was inside the HV in 15 of 23 lesions.

DISCUSSION

^{18}F-FMISO was first introduced as a promising hypoxia tracer because it is preferentially retained in cells with low oxygen pressure (*26*). ^{18}F-FMISO is lipophilic, diffusing passively through the cell membrane and taken up by both normoxic and hypoxic tissues. Once inside the cell, it may undergo a first reduction into R-NO_2, which is reversible reaction under normoxic conditions. However, at low (hypoxic) pO_2s, R-NO2 is further reduced into R-NHOH, which binds to intracellular proteins, becoming irreversibly bound. Hence, there is a relationship between ^{18}F-FMISO trapping in cells and the degree of hypoxia. The most widely used surrogate metric of tumor hypoxia in ^{18}F-FMISO PET is its TBR derived from a single late-time-point image. Investigators have reported times from 2–4 h after ^{18}F-FMISO administration (*12,27,28*). An image voxel is considered to be hypoxic if TBR exceeds a predetermined value, usually 1.2–1.4 (*18,27*). This approach, although simple to implement, may misidentify hypoxic voxels, a consequence of the slow ^{18}F-FMISO clearance from regions of high tumor perfusion. This variable uptake and slow clearance means that it is not always possible to unambiguously differentiate the impact on uptake of hypoxia and perfusion by static PET imaging alone. The acquisition of dynamic PET images combined with PKA provides a potential methodology to distinguish delivery from trapping. This approach is more complex and acquisitions more time-consuming. Nevertheless, a few studies (*15,18,21,29,30*), mainly for head and neck cancers, have demonstrated its feasibility and benefit.

TABLE 5
PKA Results for Average Muscle Time–Activity Curves

Data	*vB*	%SE *vB*	K_1 (mL/min/cm^3)	%SE K_1	K_1/k_2	%SE K_1/k_2	k_3 (min^{-1})	%SE k_3	SUV_{max}	TBR
Average	5.9E−03	45	0.031	4.2	0.87	6.7	1.1E−03	35	1.9	1.3
σ	7.1E−03	57	0.013	1.5	0.22	3.5	1.3E−03	14	0.5	0.5
Minimum	0.0E+00	13	0.013	2.6	0.62	2.6	0.0E+00	15	1.3	0.9
Maximum	2.1E−02	200	0.059	7.5	1.5	18	3.8E−03	53	2.9	2.8

Supplemental Table 4 provides patient/lesionwise results.

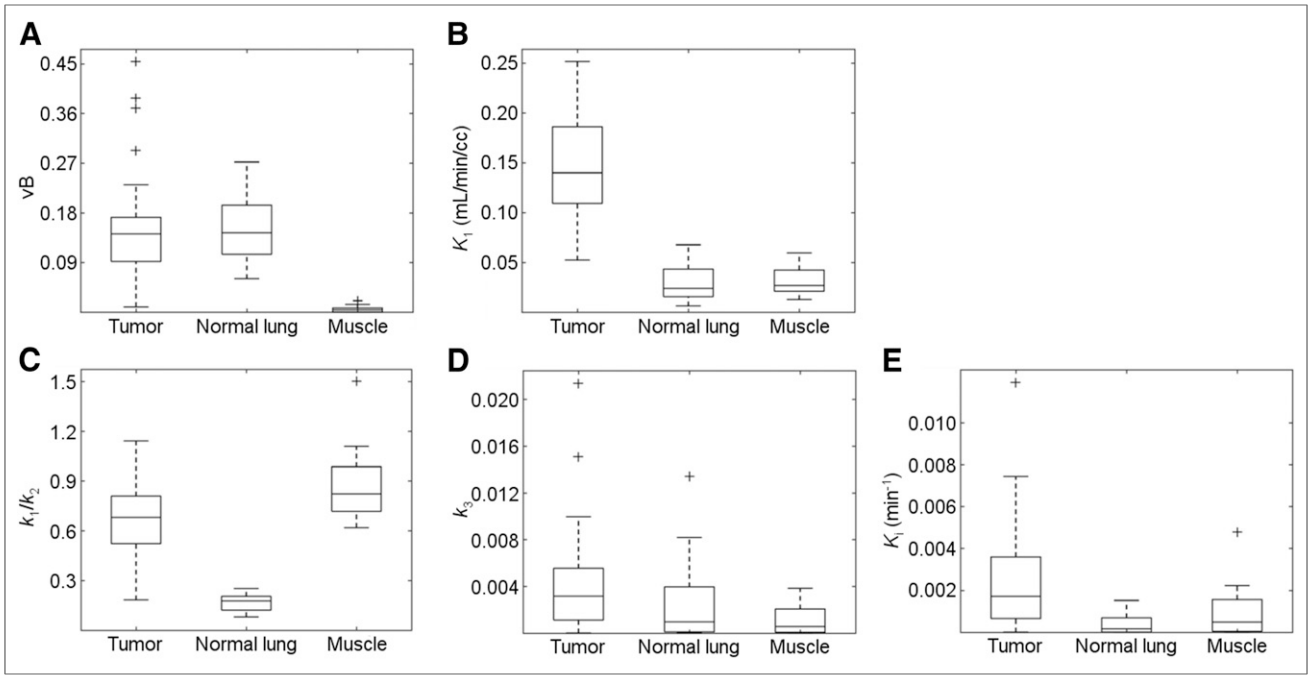

FIGURE 3. Comparison between kinetic parameters determined for the average time–activity curves of the 3 VOIs investigated (VOI_{Tumor}, VOI_{Normal}, and VOI_{Muscle}): (A) *vB,* (B) K_1, (C) K_1/k_2, and (E) K_i. Points are labeled as outliers (+) if they are farther than $1.5 \times (Q_3 - Q_1)$ from the median (midline), where Q_1 and Q_3 are the 25th and 75th percentiles of the sample data, respectively.

In this study, we performed PKA of ^{18}F-FMISO dynamic PET images of patients with NSCLC. All lesions investigated demonstrated uptake of ^{18}F-FMISO, and 31 of 34 studied showed some degree of irreversible trapping, that is, $k_3 > 0$ within the limits of the associated SE. The generic shape of the tumor and normal lung time–activity curves during early frames exhibits a sharp peak,

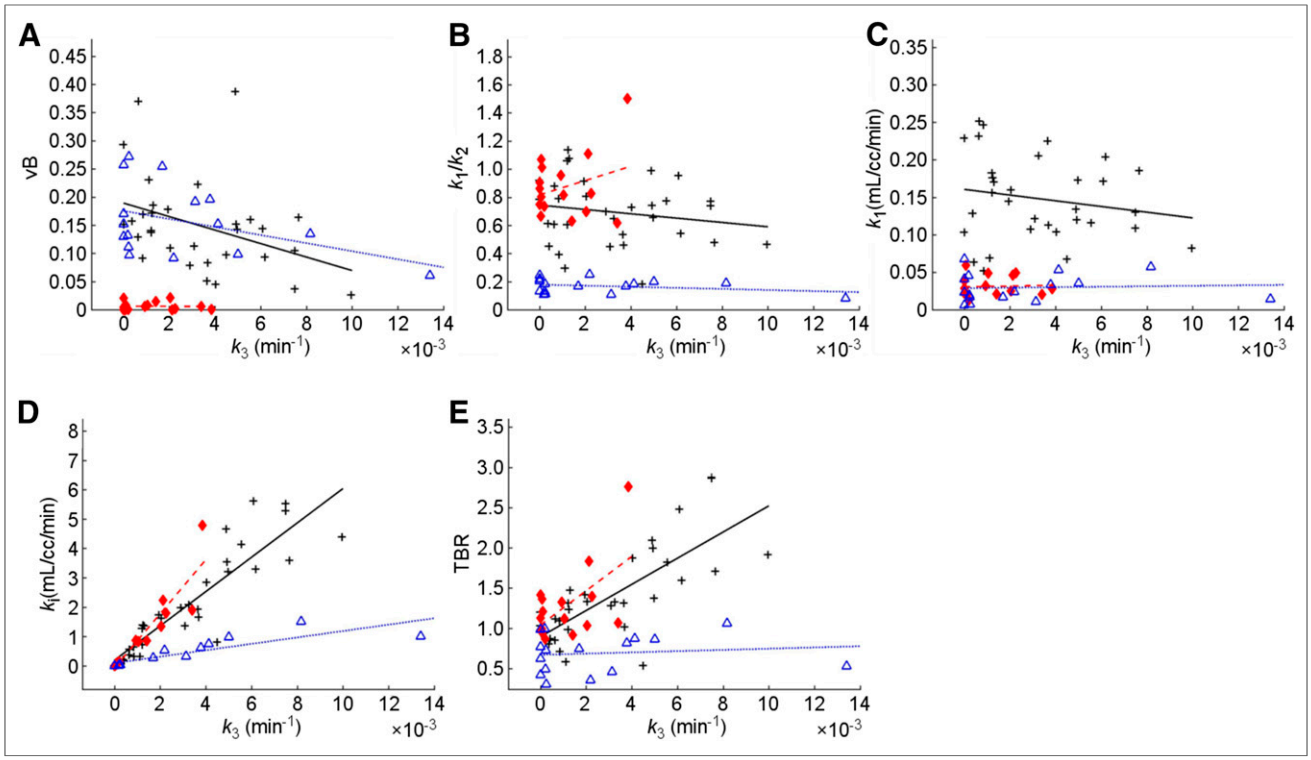

FIGURE 4. Scatterplots of k_3 versus *vB* (A), K_1/k_2 (B), K_1 (C), K_i (D), and TBR (E), for average time–activity curves: *time–activity curve*$_{Avg}$ (black), *time–activity curve*$_{Normal}$ (blue), and *time–activity curve*$_{Muscle}$ (red). Each point represents 1 lesion (some patients had multiple lesions).

TABLE 6
Correlation Results Between k_3 for Average Time–Activity Curves and Relevant Parameters Across Patients/Lesions

	Tumor		Normal lung		Muscle	
Data	R	*P*	R	*P*	R	*P*
K_1 vs. k_3	−0.17	0.32	0.58	0.19	0.28	0.32
K_1/k_2 vs. k_3	−0.22	0.33	0.13	0.65	−0.25	0.33
TBR vs. k_3	0.84	<0.001	0.41	0.13	−0.05	<0.001
Ki vs. k_3	0.91	<0.001	0.97	<0.001	0.95	<0.001
vB vs. k_3	−0.38	0.036	−0.19	0.5	−0.02	0.036

reflecting the transit of the initial injection bolus through the tissue of interest, followed by the diffusion of radiotracers from the vascular compartment into the perivascular space.

We performed PKA of lung tumors, normal lung, and muscle. The average lesion K_1, associated radiotracer delivery, resulted in the most marked difference between these tissue types among the parameters studied. Its value was larger in tumors than in either normal lung or muscle tissue by at least a factor of 1.7 in every case (range, 2–33, $\mu \pm SD = 7 \pm 7$; and range, 1.7–12, $\mu \pm SD = 6 \pm 3$, respectively), with a lower degree of overlap with the normal tissues than for any of the other parameters (Fig. 3B). The significantly ($P < 0.001$) larger K_1 values measured for lesions may reflect the abnormal tumor vasculature and easier diffusion than that of normal tissues. However, it is important to consider that the data for normal lung has not been corrected for its lower density relative to tumor and muscle. Normal lung tissue has significant components of air and blood. As a result, activity concentration is underestimated for voxels in the parenchyma. Because the air and blood fractions in the voxels are highly variable throughout the lung, corrections cannot be simply implemented via scaling. Holman et al., extending the work of Lambrou, have proposed methods for voxelwise corrections using CT_{Avg}, and showed that K_1, K_i, and SUV_{bw} were all found to be affected (*31,32*). Nevertheless, the method has not been validated and, thus, not applied in this study. Thus, it is expected that the values of K_1 and K_i reported here for normal lung would be lower had corrections been applied.

For the 2-compartment model, the rate constant k_3, representing irreversible ^{18}F-FMISO trapping, is considered a surrogate hypoxia metric. The expectation would be that such trapping would be more significant in tumors than in normal tissues. In fact, the results in this study show that whereas the average lesion k_3 is generally larger in tumors, there is some overlap across tissues; namely, 5 lesions had an average k_3 value, which was smaller than in their corresponding normal lung tissue. Three of these 5 lesions had small values of k_3 (<0.001 min^{-1}), and their oxygen status might, in accordance with their trapping rate constant, be considered closer to normoxia, as expected for normal lung tissue. However, 2 of 5 patients had values of k_3 in normal lung, indicating unexpectedly high rates of ^{18}F-FMISO trapping. The cause of this uptake in the normal lung tissue is unclear and a possible consequence of lung fibrosis, inflammation, or some other nonspecific retention in these unhealthy patients.

Single average parameter (derived from *time–activity curve*$_{avg}$) comparisons may not draw clear distinctions between tissue types and lesion subvolumes. However, it is possible to determine relationships among parameters that are indicative of the hypoxic status of tumors. The average of voxelwise parameter correlations, Figure 5, shows that k_3 increases with decreased delivery both within the tumor and across patients (*30*). This pattern is indicative of possible structural or functional differences between diseased and normal tissues, leading to a fundamentally different relationship between forward transport into the metabolic compartment and ^{18}F-FMISO trapping, as might be expected. This is further reinforced by the fact that the concordance between K_1 and k_3 becomes positive as k_3 becomes smaller. This result may imply that the magnitude of R might be indicative of weaker trapping within the tissue due to more normoxic conditions within the tumor.

Despite the theoretic advantages of modeling dynamic PET images, there are practical difficulties that may lead to inaccuracies in the estimated parameters, beyond those associated with

TABLE 7
Results of Voxelwise Correlation Analysis

	Tumor R				Normal lung R				Muscle R			
Data	K_1–k_3	K_1/k_2–k_3	TBR–k_3	K_i–k_3	K_1–k_3	K_1/k_2–k_3	TBR–k_3	K_i–k_3	K_1–k_3	K_1/k_2–k_3	TBR–k_3	K_i–k_3
Average	−0.23	−0.42	0.26	0.70	0.29	−0.22	0.23	0.85	0.29	−0.81	0.20	0.95
σ	0.39	0.39	0.44	0.29	0.25	0.26	0.26	0.08	0.43	0.22	0.35	0.09
Minimum	−0.97	−0.97	−0.52	−0.02	−0.17	−0.64	−0.17	0.70	−0.51	−0.96	−0.36	0.64
Maximum	0.72	0.62	0.85	0.99	0.76	0.40	0.88	0.96	0.90	−0.03	0.66	1.00

Statistics shown are determined for multiple patients and lesions. Supplemental Table 5 provides patient/lesionwise results.

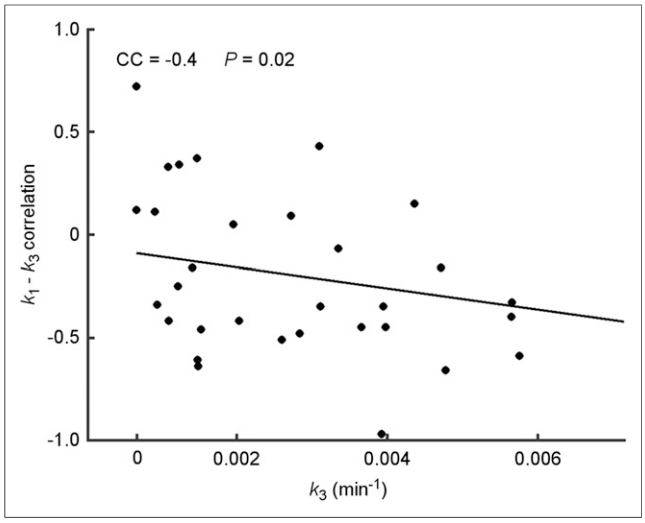

FIGURE 5. Scatterplot of K_1–k_3 voxelwise correlation versus average k_3 in VOI_{Tumor}. Each point represents 1 lesion.

errors due to statistical fluctuations. The data were acquired in 3 parts to minimize patient discomfort associated with scans longer than 45 min. In turn, it is necessary to coregister the 2 late image sets to the first to create 1 complete dynamic image series. Thus, the time–activity curve data may contain inaccuracies due to registration errors. This effect would have a larger impact on analyses of voxelwise time–activity curves than of average VOI time–activity curves. Coregistration of the ^{18}F-FDG scan to FMISO-1 for tumor delineation and segmentation may cause further inaccuracies. Additionally, it is inevitable that there will be patient motion during the scan, especially for FMISO-1, which we seek to minimize by use of the RT mold. However, especially in lung, breathing also introduces an additional complication. In this study, no correction for breathing motion was applied as all the lesions studied were assumed to be minimally affected by motion effects because they were either large or located in regions (e.g., mediastinum or upper lung lobe) in which motion is minimal. Additionally, we observed that most patients quickly fell asleep or were relaxed within a few minutes, leading to shallow breathing. Nevertheless, breathing motion corrections could improve the accuracy of results.

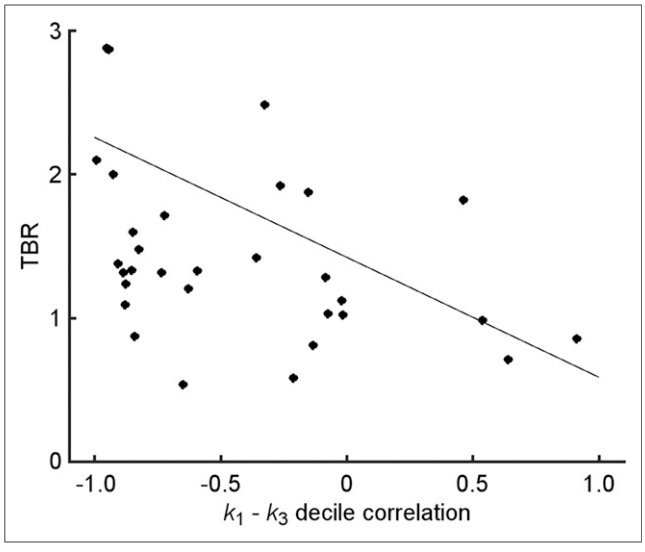

FIGURE 6. Scatterplot of TBR for VOI_{Tumor} versus K_1–k_3 decile correlation coefficient. Each point represents 1 lesion.

Although the current results provide evidence for the presence of hypoxic subvolumes within each lesion, there is currently no known method for translating a value of k_3 into an amount of hypoxia. Several authors have proposed TBR thresholds of 1.2–1.4 (*30*) as an empiric criterion for hypoxia. Twenty-three of 34 lesions studied here contained subvolumes with a TBR > 1.2, with a significant ($P < 0.001$) correlation identified between TBR and the average lesion k_3. When hypoxic regions are defined solely on the basis of TBR > 1.2, more than 30% of lesions would appear to lack macroscopic areas of hypoxia. However, 81% of those are ^{18}F-FMISO–avid ($k_3 > 0$, $P < 0.05$), showing that TBR and k_3 are not always in agreement as to determining region hypoxia. The average and maximum k_3 for the latter are significantly ($P < 0.05$) lower than for those lesions with HVs. Finally, voxelwise only 52% of lesions have a significant ($P < 0.05$) $R > 0.5$.

Finally, the results presented in this article provide further evidence that there is not always concordance between the parametric descriptors of hypoxia such as k_3 and TBR. It is possible that such discrepancies are a consequence of underlying different tumor tissue pathologies such as chronic hypoxia and ribbonlike hypoxia that is observed by immunohistochemical staining (*33*) but not resolved by PET imaging.

CONCLUSION

We have successfully performed PKA of baseline dynamic ^{18}F-FMISO PET images in a cohort of NSCLC patients. Lesions for all patients showed evidence of hypoxia as depicted by relatively increased ^{18}F-FMISO concentrations, which was corroborated by the increased k_3 values relative to those in normal lung and muscle. Because this was a prospective study, the prognostic value of our measurements could not be assessed. This investigation demonstrates the feasibility of dynamic ^{18}F-FMISO PET imaging in thoracic disease. In particular, future directions of this work include investigating the prognostic value of the rate constants and macroparameters derived from them.

Finally, although in this particular study we included only lesions minimally affected by motion, we are developing tools with which to implement corrections for breathing motion of dynamic PET. This will allow us to assess the impact of breathing motion on kinetic rate constants when studying lesions in thoracic regions with significant breathing motion effects.

DISCLOSURE

This study was supported by a grant from NIH/NCI U01 CA157442-3 (principal investigator Sadek A. Nehmeh) and the cancer center grant P30 CA008748 (principal investigator Craig B. Thompson). No other potential conflict of interest relevant to this article was reported.

REFERENCES

1. Rosenzweig KE, Amols H, Ling CC. New radiotherapy technologies. *Semin Surg Oncol.* 2003;21:190–195.
2. Sura S, Gupta V, Yorke E, Jackson A, Amols H, Rosenzweig KE. Intensity-modulated radiation therapy (IMRT) for inoperable non-small cell lung cancer:

the Memorial Sloan-Kettering Cancer Center (MSKCC) experience. *Radiother Oncol.* 2008;87:17–23.
3. Eschmann SM, Paulsen F, Reimold M, et al. Prognostic impact of hypoxia imaging with ^{18}F-misonidazole PET in non-small cell lung cancer and head and neck cancer before radiotherapy. *J Nucl Med.* 2005;46:253–260.
4. Le QT, Chen E, Salim A, et al. An evaluation of tumor oxygenation and gene expression in patients with early stage non-small cell lung cancers. *Clin Cancer Res.* 2006;12:1507–1514.
5. Nordsmark M, Bentzen SM, Rudat V, et al. Prognostic value of tumor oxygenation in 397 head and neck tumors after primary radiation therapy: an international multi-center study. *Radiother Oncol.* 2005;77:18–24.
6. Graves EE, Vilalta M, Cecic IK, et al. Hypoxia in models of lung cancer: implications for targeted therapeutics. *Clin Cancer Res.* 2010;16:4843–4852.
7. Lee NY, Mechalakos JG, Nehmeh S, et al. Fluorine-18-labeled fluoromisonidazole positron emission and computed tomography-guided intensity-modulated radiotherapy for head and neck cancer: a feasibility study. *Int J Radiat Oncol Biol Phys.* 2008;70:2–13.
8. Das SK, Miften MM, Zhou S, et al. Feasibility of optimizing the dose distribution in lung tumors using fluorine-18-fluorodeoxyglucose positron emission tomography and single photon emission computed tomography guided dose prescriptions. *Med Phys.* 2004;31:1452–1461.
9. van Lin EN, Futterer JJ, Heijmink SW, et al. IMRT boost dose planning on dominant intraprostatic lesions: gold marker-based three-dimensional fusion of CT with dynamic contrast-enhanced and ^{1}H-spectroscopic MRI. *Int J Radiat Oncol Biol Phys.* 2006;65:291–303.
10. Madani I, Duthoy W, Derie C, et al. Positron emission tomography-guided, focal-dose escalation using intensity-modulated radiotherapy for head and neck cancer. *Int J Radiat Oncol Biol Phys.* 2007;68:126–135.
11. Vanderstraeten B, Duthoy W, De Gersem W, De Neve W, Thierens H. [^{18}F]fluorodeoxy-glucose positron emission tomography ([^{18}F]FDG-PET) voxel intensity-based intensity-modulated radiation therapy (IMRT) for head and neck cancer. *Radiother Oncol.* 2006;79:249–258.
12. Koh WJ, Bergman KS, Rasey JS, et al. Evaluation of oxygenation status during fractionated radiotherapy in human nonsmall cell lung cancers using [F-18]fluoromisonidazole positron emission tomography. *Int J Radiat Oncol Biol Phys.* 1995;33:391–398.
13. Rajendran JG, Wilson DC, Conrad EU, et al. [^{18}F]FMISO and [^{18}F]FDG PET imaging in soft tissue sarcomas: correlation of hypoxia, metabolism and VEGF expression. *Eur J Nucl Med Mol Imaging.* 2003;30:695–704.
14. Rasey JS, Koh WJ, Evans ML, et al. Quantifying regional hypoxia in human tumors with positron emission tomography of [^{18}F]fluoromisonidazole: a pretherapy study of 37 patients. *Int J Radiat Oncol Biol Phys.* 1996;36:417–428.
15. Thorwarth D, Eschmann SM, Paulsen F, Alber M. A kinetic model for dynamic [^{18}F]-Fmiso PET data to analyse tumour hypoxia. *Phys Med Biol.* 2005;50:2209–2224.
16. Wang W, Georgi JC, Nehmeh SA, et al. Evaluation of a compartmental model for estimating tumor hypoxia via FMISO dynamic PET imaging. *Phys Med Biol.* 2009;54:3083–3099.
17. Milne EN. Circulation of primary and metastatic pulmonary neoplasms. A postmortem microarteriographic study. *Am J Roentgenol Radium Ther Nucl Med.* 1967;100:603–619.
18. Rajendran JG, Schwartz DL, O'Sullivan J, et al. Tumor hypoxia imaging with [F-18] fluoromisonidazole positron emission tomography in head and neck cancer. *Clin Cancer Res.* 2006;12:5435–5441.
19. Grunbaum Z, Freauff SJ, Krohn KA, Wilbur DS, Magee S, Rasey JS. Synthesis and characterization of congeners of misonidazole for imaging hypoxia. *J Nucl Med.* 1987;28:68–75.
20. Chapman JD, Franko AJ, Sharplin J. A marker for hypoxic cells in tumours with potential clinical applicability. *Br J Cancer.* 1981;43:546–550.
21. Wang W, Lee NY, Georgi JC, et al. Pharmacokinetic analysis of hypoxia ^{18}F-fluoromisonidazole dynamic PET in head and neck cancer. *J Nucl Med.* 2010;51:37–45.
22. Gupta N, Gill H, Graeber G, Bishop H, Hurst J, Stephens T. Dynamic positron emission tomography with F-18 fluorodeoxyglucose imaging in differentiation of benign from malignant lung/mediastinal lesions. *Chest.* 1998;114:1105–1111.
23. Hoekstra CJ, Hoekstra OS, Lammertsma AA. On the use of image-derived input functions in oncological fluorine-18 fluorodeoxyglucose positron emission tomography studies. *Eur J Nucl Med.* 1999;26:1489–1492.
24. Grkovski M, Schwartz J, Gonen M, et al. Feasibility of ^{18}F-fluoromisonidazole kinetic modeling in head and neck cancer using shortened acquisition times. *J Nucl Med.* 2016;57:334–341.
25. Li F, Joergensen JT, Hansen AE, Kjaer A. Kinetic modeling in PET imaging of hypoxia. *Am J Nucl Med Mol Imaging.* 2014;4:490–506.
26. Rasey JS, Grunbaum Z, Magee S, et al. Characterization of radiolabeled fluoromisonidazole as a probe for hypoxic cells. *Radiat Res.* 1987;111:292–304.
27. Fleming IN, Manavaki R, Blower PJ, et al. Imaging tumour hypoxia with positron emission tomography. *Br J Cancer.* 2015;112:238–250.
28. Muzi M, Krohn KA. Imaging Hypoxia with ^{18}F-fluoromisonidazole: challenges in moving to a more complicated analysis. *J Nucl Med.* 2016;57:497–498.
29. Casciari JJ, Graham MM, Rasey JS. A modeling approach for quantifying tumor hypoxia with [F-18]fluoromisonidazole PET time-activity data. *Med Phys.* 1995;22:1127–1139.
30. Bruehlmeier M, Roelcke U, Schubiger PA, Ametamey SM. Assessment of hypoxia and perfusion in human brain tumors using PET with ^{18}F-fluoromisonidazole and ^{15}O-H2O. *J Nucl Med.* 2004;45:1851–1859.
31. Holman BF, Cuplov V, Millner L, et al. Improved correction for the tissue fraction effect in lung PET/CT imaging. *Phys Med Biol.* 2015;60:7387–7402.
32. Lambrou T, Groves AM, Erlandsson K, et al. The importance of correction for tissue fraction effects in lung PET: preliminary findings. *Eur J Nucl Med Mol Imaging.* 2011;38:2238–2246.
33. van Laarhoven HW, Kaanders JH, Lok J, et al. Hypoxia in relation to vasculature and proliferation in liver metastases in patients with colorectal cancer. *Int J Radiat Oncol Biol Phys.* 2006;64:473–482.